Algorithms for Visual Odometry

Alex Kreimer

Algorithms for Visual Odometry

Research Thesis

Submitted in partial fulfillment of the requirements
for the degree of Master of Science in Computer Science

Alex Kreimer

Submitted to the Senate
of the Technion — Israel Institute of Technology
Kislev 5778 Haifa November 2017

This research was carried out under the supervision of Prof. Ilan Shimshoni and of Prof. Ehud Rivlin

The Technion's funding of this research is hereby acknowledged.

Contents

List of Figures

Abstract

In this work we revisit the problem of visual odometry. Visual odometry is the process of estimating the motion of the camera by examining the changes that the motion induces on the images made by it. This work has two parts: the first part proposes a novel algorithm for the visual odometry. The approach we propose exploits a scene structure typical for that seen by a moving car and is suitable for use in either the stereo or the monocular setting. We recover the rotation and the translation separately, thus dealing with two separate, smaller problems. The rotation is estimated by means of the infinite homography. The rotation estimation algorithm operates on distant image points using the 3-D to partition them into the distant and the near-by ones. We start with an initial estimate and then refine it using an iterative procedure. After the rotation is compensated for, the translation is found by means of the 1-point algorithm in the stereo setting and epipole computation for pure translational motion in the monocular setting. We evaluate our algorithm on the KITTI dataset [Gei12]. The second part of this work explores a method to recover the scale of camera motion. The size of a translation vector for a single moving camera is not directly observable, although is desirable. Stereo, scene/camera prior assumptions were used in the past to recover the translation size. We argue that the required information is present in the images and explore a number of ways to learn it. We experiment with both "legacy" shallow learning methods and hand-crafted features as well as end-to-end learning methods based on the convolutional neural networks.

Chapter 1

Introduction

Visual odometry refers to the problem of recovering camera motion based on the images taken by it. This problem naturally occurs in robotics, wearable computing, augmented reality and automotive.

Wheel odometry, recovers the motion of the vehicle by examining and integrating the wheel turns over time. In a similar manner, visual odometry operates by estimating relative motion of the camera between subsequent images by observing changes in them. Later, these estimates are combined into a single trajectory. Just as in wheel odometry, visual odometry is subject to error accumulation over time. Contrary to wheel odometry, visual odometry is not affected by wheel slip in a rough terrain. Visual odometry is able to produce motion estimates with errors that are lower than those of the wheel odometry. Another advantage of visual odometry is that cameras are low cost and low weight sensors. All these make visual odometry a viable supplement to other motion recover methods such as global positioning systems (GPS) and inertial measurement units (IMUs).

Visual odometry becomes a harder problem as the amount of detail in the images diminishes. The images should have sufficient overlap and the scene needs to be illuminated. In the stereo setup, the scene must be static or the images taken at the same time. Also, the video processing incurs a computational burden.

Visual odometry is an active fields of research with a large amount of published work. We review only the most pertinent works. [FS12] provides a more complete survey.

Similar to [PPFM15] we partition visual odometry algorithms by four traits:

1. Feature-based vs direct

2. Global vs local

3. Filter based vs bundle adjustment based

4. Monocular vs stereo

Visual odometry algorithms use large number of corner detectors (e.g., Moravec [Mor80], Harris [HP87], Shi-Tomasi [ST94], Fast [RD06]) and blob detectors (e.g., SIFT [Low04], SURF [BTG06]). Corners are faster to compute and usually are better localized, while blobs are more robust to scale change. The choice of a specific feature point depends mainly on the images at hand. Motion estimation results for different feature points are presented in [Gov09]. In this work we choose Harris [HP87] corners, but this choice is not crucial. We view the feature point choice as a parameter, which needs to be determined from the data (e.g., by cross-validation).

The features are either tracked [HFF09] or matched [GZS11] (i.e., freshly detected in each new frame) between subsequent images. While the early works chose to track features, most of the current works detect and match them. The output of this stage are pairs of the image features, which are the projections of the same 3-D point.

Matched features are used as an input for a motion estimation procedure. Whether the features are specified in 2-D or 3-D, the estimation procedures, may be classified into 3-D-to-3-D [MS06], 3-D-to-2-D [GZS11] and 2-D-to-2-D [Nis04]. Most of the early works were of the 3-D-to-3-D type. More recent works [Nis04] claim that this approach is inferior to the latter two. Popular techniques that participate in most algorithms in some way are essential matrix estimation and (possibly) its subsequent decomposition [Nis04], perspective 3-point algorithm [KSS11], and re-projection error minimization [GZS11].

Global methods [KM07], [NLD11] keep the map of the environment and make sure that motion estimates are globally consistent with this map, while local methods do not. Some local methods [BYK13] also keep track of a (local) map, but the underlying philosophy is different: global vs local. Global methods are usually more accurate since they make use of a vast amount of information (which, of course, comes at a computational price). Note that accuracy does not imply robustness, since outliers that made their way into the map may greatly skew subsequent pose estimates.

Methods that explicitly model system state uncertainty tend to use filtering mathematical machinery, e.g., [KAS10], [OMSM03], [KRD08]. Another alternative to maintain map/pose estimate consistency is to use the bundle adjustment approach [TMHF99]. Monocular systems [SCG13] make use of a single camera, while stereo systems [GZS11] rely on a calibrated stereo rig. In the monocular setup the translation of the camera may only be estimated up to scale, while in stereo all six motion parameters may be recovered. An additional advantage of the stereo setup is that more information is available at each step, which may be one of the reasons why stereo algorithms perform better.

The rest of this document is organized in two chapters. The first chapter presents a novel algorithm for monocular visual odometry. The algorithm takes a divide and conquer approach. It first computes the rotation and then a translation of the camera. We begin with preliminaries and notation, proceed to describe the algorithm in stereo and in mono and conclude with experimental results. We show, that our algorithm compares favorably with a chosen baseline. The second chapter revisits a problem of scale in monocular camera motion estimation. We propose a method based on statistical machine learning to estimate the absolute scale of a single camera motion. We evaluate random forest, convolutional neural networks and recurrent neural network based models. In the preliminaries, we briefly discuss these models and how we apply them to the problem of scale estimation. In the experiments section, we describe feature extraction, model training and prediction. We show that fully convolutional network, called FlowNet performs best, out of selected models. The final chapter, makes conclusions and notes possible directions for future work.

Chapter 2

Infinite Odometry

2.1 Introduction

In this work we present a novel algorithm for camera motion estimation. The novelty of the algorithm is in camera rotation estimation procedure. We rely on the fact that for scene points that are infinitely far from the camera, the motion of the projected (image) points may be described by an homography (the infinite homography). For distant points this assumption is nearly true. Our algorithm starts by partitioning the scene points into two sets: distant and near-by. Then, camera rotation is estimated from the distant points and, subsequently, the translation is recovered from the near-by points.

We present two versions of the algorithm: one for the monocular and the other for the stereo settings. These versions differ in the way we partition points into the distant and the near-by ones and in the way the algorithms estimate translation.

With respect to the classification of the visual odometry methods given in the introduction, our work is local, feature based, stereo odometry. We do not use bundle adjustment, however the results of our algorithm may be subsequently improved with some form of bundle adjustment.

The outline of the our method:

1. Feature detection. We use Harris [HP87] corners.

2. Feature matching. The matching is done both across the stereo pair images as well as previous vs. current pair. We enforce epipolar constraint, chierality and use circle heuristics similar to [GZS11] to reject outliers.

3. Partition the scene points into two sets: distant and near-by.

4. Estimate the rotation of the camera from the distant points.

5. Estimate the translation of the camera from the near-by points.

We choose the work [GZS11] as our baseline (our implementation of their work). The results in the Section 3.6.4 show that on the KITTI dataset our rotation estimation method outperforms the baseline.

2.2 Preliminaries and Notation

2.2.1 Image Point Mapping Related to Camera Motion

Suppose the camera matrices are those of a calibrated stereo rig P and P$'$ with the world origin at the first camera

$$\mathrm{P} = \mathrm{K}[\mathrm{I} \mid 0], \quad \mathrm{P}' = \mathrm{K}'[\mathrm{R} \mid \mathbf{t}]. \tag{2.1}$$

Consider the projections of a 3D point $\mathbf{X} = (X, Y, Z, 1)^T$ into the image planes of both views:

$$\mathbf{x} = \mathrm{P}\mathbf{X}, \quad \mathbf{x}' = \mathrm{P}'\mathbf{X}. \tag{2.2}$$

If the image point is normalized as $\mathbf{x} = (x, y, 1)^T$ then

$$\mathbf{x}Z = \mathrm{P}\mathbf{X} = \mathrm{K}[\mathrm{I} \mid 0]\mathbf{X} = \mathrm{K}(X, Y, Z)^T.$$

It follows that $(X, Y, Z)^T = \mathrm{K}^{-1}\mathbf{x}Z$, and:

$$\begin{aligned} \mathbf{x}' &= \mathrm{K}'[\mathrm{R} \mid \mathbf{t}](X, Y, Z, 1)^T & (2.3)\\ &= \mathrm{K}'\mathrm{R}(X, Y, Z)^T + \mathrm{K}'\mathbf{t} & (2.4)\\ &= \mathrm{K}'\mathrm{R}\mathrm{K}^{-1}\mathbf{x}Z + \mathrm{K}'\mathbf{t}. & (2.5)\end{aligned}$$

We divide both sides by Z to obtain the mapping of an image point $\mathbf{x}$ to image point $\mathbf{x}'$

$$\mathbf{x}' = \mathrm{K}'\mathrm{R}\mathrm{K}^{-1}\mathbf{x} + \mathrm{K}'\mathbf{t}/Z = \mathrm{H}_\infty\mathbf{x} + \mathrm{K}'\mathbf{t}/Z = \mathrm{H}_\infty\mathbf{x} + \mathbf{e}'/Z. \tag{2.6}$$

H_∞ is the infinite homography that transfers the points at infinity to the points at infinity. If $\mathrm{R} = \mathrm{I}$ (e.g., pure translation) the point $\mathbf{x}$ will undergo a motion along a corresponding epipolar line:

$$\mathbf{x}' = \mathbf{x} + \mathrm{K}'\mathbf{t}/Z = \mathbf{x} + \mathbf{e}'/Z. \tag{2.7}$$

If $\mathbf{t} = \mathbf{0}$ the motion of the point may be represented by a homography:

$$\mathbf{x}' = \mathrm{H}_\infty\mathbf{x}. \tag{2.8}$$

In a general case the mapping of an image point $\mathbf{x}$ into $\mathbf{x}'$ may be viewed as a two step process: transformation by a homography which simulates a pure rotational motion of the camera followed by an offset along the epipolar line which simulates a pure translational motion of the camera, see Figure 2.1.

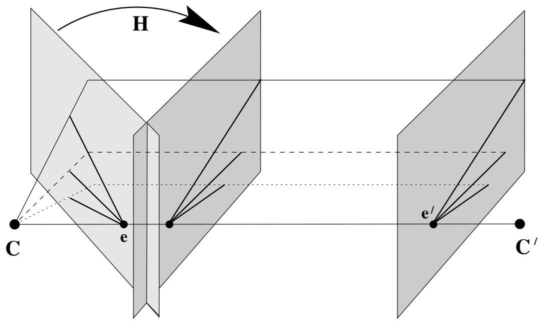

Figure 2.1: (Adapted from [HZ04]) The effect of the camera motion on the image points may be viewed as a two-step process: mapping by a homography H_∞ followed by a motion along the corresponding epipolar lines.

2.3 Motion Estimation

Our strategy to attack the problem is to separate it into two smaller sub-problems: rotation estimation and translation estimation. The algorithm relies on the ability to partition the scene points into two sets: the distant and the near-by ones. The distant points are used for rotation estimation while the near-by ones take part in the translation estimation.

First, the stereo algorithm is presented, followed by the monocular one. The main difference is in the translation estimation part. While it is possible to implement a stereo-like algorithm in the monocular setting as well, it suffers from the scale drift. Thus, we propose a different technique.

2.3.1 Stereo

Partitioning the points To partition the points in the stereo case we hard-threshold their Z-coordinates (the threshold is a parameter of the algorithm). The depth of the points was computed by stereo triangulation.

Rotation Estimation: We use distant points to estimate rotation R (i.e., near-by points do not take part in rotation estimation). As Eq. (2.6) states:

$$\mathbf{x}' = \mathrm{KRK}^{-1}\mathbf{x} + \mathrm{K}\mathbf{t}/Z. \tag{2.9}$$

The total motion of the feature point in the image plane may be viewed as a two-step process (the order is not important): transformation by homography $\mathrm{H}_\infty = \mathrm{KRK}^{-1}$ followed by displacement along the line defined by the epipole e' and the point $\mathrm{H}_\infty\mathbf{x}$. The magnitude of the displacement along the epipolar line depends on the camera translation and the inverse depth of the point, see Figure 2.2.

Our estimation algorithm consists of initialization and non-linear refinement.

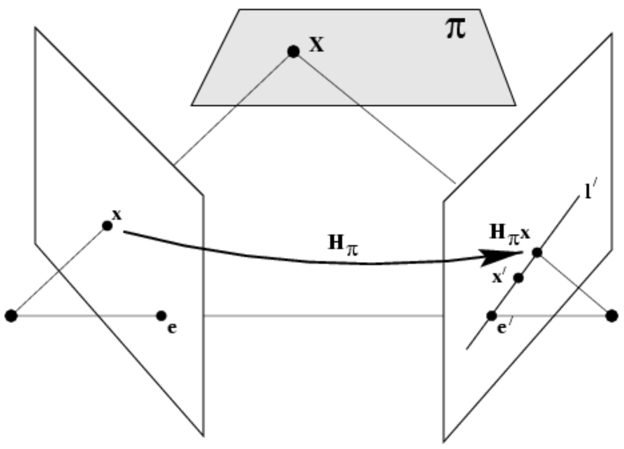

Figure 2.2: (Adapted from [HZ04]) The homography H_π transfers the point onto a corresponding epipolar line. The displacement along the epipolar line depends on the inverse depth of the point and the camera translation magnitude.

Initialization: to compute the initial estimate of the rotation parameters we assume that for the distant points (s.t., $\|\mathbf{t}\|/Z \ll \|\mathrm{H}_\infty \mathbf{x}\|$):

$$\mathbf{x}' \approx \mathrm{KRK}^{-1}\mathbf{x}. \tag{2.10}$$

This assumption is justified by the fact that for the distant points the displacement along the epipolar line is small. We multiply both sides of Eq. (2.10) by K^{-1} and denote $\mathbf{u}' = \mathrm{K}^{-1}\mathbf{x}$ and $\mathbf{u} = \mathrm{K}^{-1}\mathbf{x}$:

$$\mathbf{u}' = \mathrm{K}^{-1}\mathbf{x}' \approx \mathrm{RK}^{-1}\mathbf{x} = \mathrm{R}\mathbf{u}. \tag{2.11}$$

Since $\mathbf{u}$ and $\mathbf{u}'$ are projective quantities, only their directions are of importance, we normalize them to unit length and denote normalized quantities by $\tilde{\mathbf{u}}$ and $\tilde{\mathbf{u}}'$ respectively. We choose a sample of n points ($n = 3$) and stack them as columns of matrices $\tilde{\mathrm{U}}$ and $\tilde{\mathrm{U}}'$ respectively. We search for R that solves the following minimization problem:

$$\underset{\mathrm{R}}{\operatorname{argmin}} \|\tilde{\mathrm{U}}' - \mathrm{R}\tilde{\mathrm{U}}\|_2. \tag{2.12}$$

Eq. (2.12) is known as the absolute orientation problem (see e.g., [Hor87]) and its solution provides an initial estimate for the subsequent non-linear optimization problem.

Refinement: The idea of the refinement is this: the residual vector $\mathrm{H}_\infty\mathbf{x} - \mathbf{x}'$ may be viewed as a sum of a vector orthogonal to the epipolar line and the vector parallel to it. We search for the camera rotation that ignores the parallel component (we view it as a “legal” bias) while trying to minimize the orthogonal one. We define the point residual as the orthogonal distance to the corresponding epipolar line and minimize the sum of squared residuals for all points. We do so, because, as Eq. (2.6) suggests, after we compensate for a rotation, the point is still allowed to move along the epipolar line.

Consider the objective:

$$\mathrm{R}(\mathrm{v},\theta) = \underset{v,\ \theta}{\operatorname{argmin}} \sum_{i=1}^{N} {r_i}^2 \quad \text{s.t.} \quad r_i = n_i \cdot (\mathbf{x}_i' - H_\infty(v,\theta)\mathbf{x}_i) \\ \text{where } n_i = (\mathrm{F}\mathbf{x}_i)_\perp \tag{2.13}$$

$\mathrm{H}_\infty(v,\theta) = \mathrm{KR}(\mathrm{v},\theta)\mathrm{K}^{-1}$ is the homography that transforms the image points in Eq. (2.6). It depends on a known camera intrinsic matrices K and a rotation matrix R. We choose to parameterize the rotation by an angle θ and an axis v. F denotes the fundamental matrix that corresponds to two subsequent stereo rig poses and is computed elsewhere. $\mathrm{F}\mathbf{x}_i$ denotes the epipolar line that corresponds to $\mathbf{x}_i$ in the second image and $(\mathrm{F}\mathbf{x}_i)_\perp$ is the normal to this line. We solve the minimization problem (2.13) by means of the Levenberg-Marquardt optimization algorithm.

To make the estimation robust we wrap the initialization procedure into the RANSAC iterations. We choose the strongest consensus estimate and its support set as an input for the solution of the Eq. (2.13).

Translation Estimation (1-point algorithm) To estimate the translation we use only the near-by points. First, we triangulate these points in the previous stereo pair to obtain their 3-D locations, and then iteratively minimize the sum of reprojection errors into the current frame.

The reprojection of point $\mathbf{X} = (X, Y, Z, 1)^T$ into the current left image is given by:

$$\pi^{(l)}(\mathbf{X};\mathbf{t}) = K\Big[\mathrm{R} \mid \mathbf{t}\Big]\mathbf{X}. \tag{2.14}$$

and the reprojection of the same point into the current right image (b is the baseline of the stereo-rig) is given by:

$$\pi^{(r)}(\mathbf{X};\mathbf{t}) = K\Big[\mathrm{R} \mid \mathbf{t}\Big](\mathbf{X} - (b,0,0,0)^T), \tag{2.15}$$

We use the Levenberg-Marquardt algorithm to iteratively minimize the sum of squared reprojection errors (starting from $\mathbf{t} = \mathbf{0}$):

$$\|\mathbf{x}' - \pi^{(l)}(\mathbf{X};\mathbf{t})\|^2 + \|\mathbf{x}' - \pi^{(r)}(\mathbf{X};\mathbf{t})\|^2. \tag{2.16}$$

There are three unknown parameters, since $\mathbf{t} = (t_x, t_y, t_z)^T$, thus a single 3-D point provides enough constraints to determine $\mathbf{t}$.

2.3.2 Mono

The stereo setup has an advantage over the monocular one in the sense that it provides the algorithm with more information (e.g., the calibration and the additional image at each camera position). These advantages come at a price, e.g., the cameras need to be synchronized and the computational resource requirements climb. These make monocular setups and the related algorithms more attractive. In the following section we present the version of our algorithm, adapted for the monocular setup.

Given two sets of matching image points $\mathbf{x}_i, \mathbf{x}'_i$ from two subsequent frames I_1, I_2 respectively, we estimate the camera motion between these frames. Similar to the stereo algorithm in Section 2.3.1 the algorithm first partitions the points and then estimates the rotation followed by the estimation of the translation direction (it is well known that the magnitude of the camera translation is unavailable in the monocular setting).

Partitioning the points To estimate the rotation of the camera as in the Eq. (2.3), it is required to partition the set of the image points into the distant ones and the near-by ones. While in the stereo setting we may triangulate the points and threshold their depths, in the monocular setting this can not be done. This section proposes a method to perform the aforementioned partition in the monocular setting.

Consider the subsequent images I_1, I_2, I_3 taken by a moving camera at the locations O_1, O_2 and O_3 respectively. We assume the image points $\mathbf{x}_i$ in I_1 are known to be distant relative to the camera at O_1. The magnitude of the camera translation is small relative to the distant points depths, thus we assume that these points are distant w.r.t. the camera at O_2 and O_3 as well. Some of these points will be lost in I_3, thus it is desirable to known which of the points tracked from I_2 to I_3 (which are not part of $\mathbf{x}_i$'s) are distant (denote these by $\mathbf{y}_j$).

The real baselines $t_1 = \|O_1 - O_2\|$ and $t_2 = \|O_2 - O_3\|$ are unknown and thus we can not use them to obtain real depths of the points.

We use the following procedure to classify the newly tracked points in I_2 as distant:

1. Set $t_1 = 1$ and triangulate the distant points $\mathbf{x}_i$ to obtain the depths Z_i
2. Set $t_2 = 1$ and triangulate the points $\mathbf{y}_j$ to obtain the depths Z_j
3. Classify the point y_j to be distant if $Z_j > \min_i Z_i$.

While the assumption $t_1 \approx t_2$ is acceptable for the KITTI dataset, it may be improved on by computing the t_1/t_2 ratio (by minimizing the reprojection errors of $\mathbf{x}_i$ into I_3, similar to the translation estimation described in the Section 2.3.1).

To initialize the monocular algorithm we may further assume that the initial motion is a pure translation and thus the points with small disparity are the distant ones (disparity being the magnitude of the motion in the image plane).

Rotation Estimation is exactly as in the Section 2.3.1. Denote the estimated rotation by R and the corresponding homography by H.

Translation Estimation is as follows. Compensate the rotation by computing $\mathbf{y}_i = \mathrm{H}_\infty \mathbf{x}_i$. We optimize over the location of the epipole e and minimize the orthogonal distances of the points to their corresponding epipolar lines:

$$\operatorname*{argmin}_e \sum_i d(l_i, \mathbf{y}_i) + d(l_i, \mathbf{x}'_i) \text{ s.t. } d(e, l_i) = 0 \text{ while } l_i = \operatorname*{argmin}_l d(l, \mathbf{x}'_i) + d(l, \mathbf{y}_i) \tag{2.17}$$

We define the epipolar line l_i to be the line that passes through the epipole and its distance to $\mathbf{x}'_i$ and $\mathbf{y}_i$ is minimal. $d(l, \mathbf{x})$ denotes the distance from the line l to the point $\mathbf{x}$. The epipole provides us with the translation direction of the camera.

2.4 Experimental Results

2.4.1 The Choice of Features

We chose to evaluate our algorithm on the KITTI dataset [Gei12], which is a de-facto standard for the visual odometry research works.

Feature Detector/Descriptor: We use Harris [HS88] corner detector. It is fast, well localized and (most important) Harris corners are abundant in urban scenes we work with. We detect corners in each new image and then match them to obtain putative matches. We tune sensitivity threshold of the detector in such a way, that we are left with about five hundred putative matches after matching and pruning. We extract a square patch of 7×7 pixels centered at the corner point and use this vector as feature descriptor.

We would like to point out that our method may be used with any feature detector that would allow to match features across images. The choice of feature detector should be viewed as a parameter to the algorithm and mainly depends on the images at test.

Feature Matching: We use sum-of-square differences (SSD) of feature descriptors as a metric function when matching features. For each feature we choose a single best match w.r.t. the metric function in the other image. We employ a number of heuristics to prune outliers:

- Reciprocity: features a and b match only if a matches b and b matches a
- Epipolar constraint: we work with calibrated stereo pair. When we match features across images of stereo pair, the search is one-dimensional, i.e., along the horizontal epipolar line. This heuristic is not used when matching features across subsequent frames.

- Chierality (visibility): also used when matching features across stereo pair images. We triangulate the features to obtain the 3-D point and keep the match only if the 3-D point is visible in both cameras.
- Circular match: similar to [GZS11] we keep only those matches that form a circle.

2.4.2 Experimental Results

The Tables 2.1 and 2.2 present the results of the experiments for the KITTI dataset. The columns denote the number of the sequence. The rows denote the algorithm: SS is the baseline, HX is the stereo version of the algorithm, HG is the monocular version. The numbers are the mean error for the corresponding sequence with the last column is the mean error for the dataset. The error computation method is described in [Gei12].

Stereo In this set of experiments we ran our algorithm in its stereo mode as described in the Section 2.3.1. Table 2.1 and 2.2 present the rotation and the translation errors respectively in the row HX. The columns marked bold are those that our algorithm outperforms the baseline (on 9 of 11 sequences). The results show that our algorithm improves the rotation results over the benchmark algorithm and successfully competes with it in the translation estimation.

Mono In an additional set of experiments we ran our algorithm in a monocular mode. Monocular motion estimation lacks a scale parameter. In order to compare the results we set the scale of the translation to be that of the stereo algorithm. Feature point selection/partition was done without using any stereo information and the motion estimation was done as explained in the Section 2.3.2.

2.5 Conclusions and Discussion

This work presents a novel visual odometry algorithm. The novelty of the algorithm is in its rotation estimation method. The rotation is estimated by means of the infinite homography. The algorithm may be used both in the stereo and in the monocular setting.

The strengths of the presented algorithm are in its ability to split the motion estimation problem into two smaller problems and to operate directly on the image points instead of on the computed 3-D quantities. Splitting the problem helps because each sub-problem is easier to solve. The ability to partition the points into the distant and the near-by ones is what allows us to separate the rotation and the translation estimation.

The stereo version of the algorithm shows better performance, but the monocular version has the advantage of being a more practical one. Indeed the authors in [Gei12]

Table 2.1: Rotation errors for the KITTI sequences [deg/m]

	00	01	02	03	04	05	06	07	08	09	10	mean
SS	3.95e-04	1.98e-04	4.11e-04	1.07e-03	8.03e-04	3.49e-04	4.72e-04	2.96e-04	3.69e-04	3.44e-04	4.82e-04	4.71e-04
HX	**2.70e-04**	**1.75e-04**	**4.10e-04**	**6.51e-04**	**6.04e-04**	3.95e-04	**3.77e-04**	**2.37e-04**	**3.23e-04**	**3.22e-04**	5.66e-04	**3.93e-04**
HG	8.72e-04	3.89e-04	6.28e-04	1.07e-03	5.99e-04	6.96e-04	3.31e-04	8.12e-04	8.13e-04	6.82e-04	5.23e-04	6.74e-04

Table 2.2: Translation errors for the KITTI sequences %

	00	01	02	03	04	05	06	07	08	09	10	mean
SS	4.40e+00	9.25e+00	4.03e+00	1.22e+01	5.06e+00	2.80e+00	4.37e+00	2.21e+00	4.12e+00	5.25e+00	5.60e+00	5.39e+00
HX	3.07e+00	1.08e+01	3.80e+00	7.94e+00	3.82e+00	4.06e+00	3.99e+00	1.67e+00	3.28e+00	3.77e+00	5.65e+00	4.72e+00
HG	1.21e+01	1.48e+01	8.72e+00	1.33e+01	8.62e+00	8.37e+00	4.46e+00	7.93e+00	9.76e+00	1.16e+01	8.36e+00	9.82e+00

report that they re-calibrate the cameras before each drive, which is hardly possible in real world installations.

Chapter 3

Monocular Scale

3.1 Introduction

Recovering camera 6-DOF ego-motion from images is a well studied problem. It arises in various practical contexts (e.g. virtual/augmented reality application, autonomous or aided navigation, etc.). The problem was studied in both stereo and the monocular setups. To recover the full 6-DOF motion, the previous works resorted to the stereo setup, used auxiliary sensors (e.g. IMU) or rely on the planar motion assumption. All of these have their drawbacks: stereo pairs are fragile and require careful calibration procedures, additional sensors are not always available and also require calibration, scene assumptions don't always hold. Motion estimation from images of a single moving camera is probably the hardest setup, as well as the most desirable one, because of its simplicity. It is well known that the translation scale parameter is not directly observable for a motion of a single camera.

We argue, that for natural scenes the scale information is present in the images (see e.g. Figure 3.7). We propose to apply statistical machine learning techniques to learn the monocular scale. We experiment with random forest, convolutional neural nets and recurrent neural nets. In the following sections we present an overview of the existing works in the field, describe our method and present the experimental results.

3.2 Related work

Geometric methods Previous geometric works in monocular scale estimation may roughly be divided into ground plane and non-ground plane methods.

Ground plane methods rely on the following assumptions: camera height (a distance from the camera principle center to the ground plane) is known to the method, a predefined region of the image (usually the one in front of the camera in the world) contains projections of the ground plane points, the ground is in front of the camera. These assumptions allow to properly scale the camera motion vector.

Ground planes in consecutive images are commonly related by a homography matrix.

Homography matrix may be estimated from a set of sparse correspondences (e.g., [SC14]) or from dense region matching as in [FSBM17]. The sparse correspondence method is sensitive both to outliers and to scarcity of features in the ground region. Dense region methods tend to fail when the region deviates from being planar (especially in curb areas). Modern methods parameterize the homography through camera and plane parameters rather than plane matrix entries. This allows to prevent homography decomposition step that introduces additional errors, see e.g., [ZDL16], that contributes a divide-and-conquer approach, where they decompose the ground plane homography into the structure and the motion parameters. Their optimization step is based on this division. [KRC$^+$11] take a more SLAM-like approach by collecting and keeping track of a constand number of ground-plane features which they use to refine the scale. [GSL15] complement the ground plane estimation based on the structure from motion techniques with vanishing point estimation which renders the algorithm robust in urban scenarios. [FSBM17] considers both dense and sparse cues for ground plane estimation. This makes their method robust toward varying availability and distribution of trackable ground structure. They parameterize and optimize over the motion parameters directly, instead of optimizing the ground plane homography. Furthermore they use classifiers based on e.g., moments and residuals to reject scale outliers.

The idea of using non-ground objects to estimate scale was explored by [SC14] and [FKM16]. These works employ object size change as an additional cue to determine the correct scale.

Another category of works proceed by making assumptions on the camera motion. In [GGPG12] the authors assume head-mounted camera and relate the vertical camera oscilation frequence to the step length and, subsequently, to person height, which allows full 6DOF motion estimation. [SFPS09] assumes that the vehicle adheres to the Ackerman steering principle and exploit the non-holomicity of its motion, to compute the scale.

Learning methods There are a number of works that use machine learning approaches to solve the 6DOF visual odometry. Optical flow is used to train k-nearest neighbour, Gaussian processes and support vector machines in [RNKB08], [GR13], [CCVR14] respectively. [WCWT17] shows that visual odometry may be addressed in the end-to-end fashion, using the deep learning techniques. The authors use CNN to learn the geometric feature representation and the recurent neural networks to model sequential motion dynamics. In [MS17], the authors use optical flow images as CNN input to learn and infer camera motion. Authors in [MAD$^+$16] also propose to train a CNN.

Recent work of [FMP17] (our work was done independently) performs similar experiment to ours. They train a convnet to predict camera translation vector magnitude (referred to as “speed”). Their work makes two major contributions: a method to learn a camera “speed” and a regulalization method to incorporate such speed prediction into a bundle adjustment procedure. Their learning procedure is very similar to the one proposed in this work. The novel regularization they propose penalizes differences between the estimated and measured speed of the camera during the open-loop trajectory. They are able to produce a virtually scale drift free monocular SLAM trajectories using the combination of the above two procedures. We compare to their results.

3.2.1 Our method

We assume that a single camera moves through space and takes images. We treat the initial camera pose (at time $t = 0$) as the world coordinate frame. We denote the pose of the camera at time t by $\hat{\mathbf{T}}_t$ described by the rotation matrix $\hat{\mathbf{R}}_t$ and the translation vector $\hat{\mathbf{t}}_t$ as seen in the world coordinate frame. We denote camera image taken at time t by I_t. To facilitate the discussion, we also introduce notation for camera pose $\mathbf{T}_t = [\mathbf{R}_t \mid \mathbf{t}_t]$ as seen from the coordinate frame associated with camera pose at time $t-1$. Most of the time, we will omit the time index, since its clear from the context. By translation scale (or simply, scale) we refer to the norm of the translation vector $\mathbf{t}$ (e.g., $s = \|\mathbf{t}\|$)

We pose the scale estimation problem as a regression problem and search for a good regressor model. We evaluate random forest, two different convnet architectures and a recurrent nerual network.

3.3 Random forest

3.3.1 Decision trees

In this section we briefly describe tree-based methods for regression. These involve splitting the feature space into a number of small regions. The prediction for a sample is made by computing a mean or a mode of training samples that belong to the same region. Since the set of rules used to split the feature space into smaller regions may be described by a tree, these methods are referred to as *decision tree* methods.

Building a decision tree may be described by a two step procedure:

1. Split the feature space, e.g., the set of all possible values for $X_1, X_2, \ldots, X_n$ into J distinct regions $R_1, R_2, \ldots, R_J$.

2. For every sample that belongs to the regions R_i we make the same prediction, which is a mean of the responses of training samples that belong to this region.

The regions R_i are usually chosen to be multidimensional boxes (axis aligned). We would like to find such a partition of the feature space that minimizes

$$\sum_{j=1}^{J} \sum_{x \in R_j} (x - \bar{y}_j)^2, \tag{3.1}$$

Where y_j denotes the mean of the response values of the samples in region R_j. Unfortunately, solving the optimization problem 3.1 is computationally hard. Usually it is replaced with a greedy algorithm, called *recursive binary splitting.* This approach starts at the top of the tree and greedily chooses the best split at that point that minimizes the variance of its sub-trees. To be more precise, for each j and s we define the hyper-planes:

$$R_1(j,s) = \{X|X_j < s\} \quad \text{and} \quad R_2(j,s) = \{X|X_j \geq s\}, \tag{3.2}$$

We seek such j and s that minimize the equation:

$$\sum_{i:x_i \in R_1(j,s)} (x_i - y_{R_1})^2 + \sum_{i:x_i \in R_2(j,s)} (x_i - y_{R_2})^2, \tag{3.3}$$

Where y_{R_1}, y_{R_2} are the average responses of the samples in $R_1(j,s), R_2(j,s)$ respectively. Once we found the j and s we recursively split each sub-tree in a similar manner. The process is repeated until a stopping criterion (e.g., number of nodes in the leaf) is reached.

3.3.2 Bagging

Decision trees tend to suffer from *high variance.* This means that if we split the training set into a number of random subsets and fit random tree into each sub-sample, we would likely to get much different answers from these trees when asked the same question. It is known that the variance of a mean of a set of independent random variables is $\frac{1}{n}$. Thus, in order to improve the variance of the estimator, it is possible to fit n estimators, each to its training-set and the average their predictions. Since, usually, we don't have n training sets, we would use *bootstrapping* (e.g., sample independently with replacement from the data set).

3.3.3 Random Forest

The random forest suggests an additional improvement over bagging, by decorrelating the random trees. The issue they attempt to address is this: lets say there is a very dominant feature w.r.t. to task at hand for a given data-set. Bagging ensures that we use different training sets, but yet, most trees will tend to first split on this dominant feature. In this case the trees will resemble each other. In random forest, the trees are constructed by using only a subset of features (e.g., $m = \sqrt{p}$). This means that at calculating the splits, the algorithm is allowed to consider only a subset of features.

3.4 Convolutional Neural Networks

Convolutional neural networks (CNN) leverage the availability of the computational power and the abundance of data. CNN have become a method of choice in a number of computer vision areas (e.g., image classification [KSH12] [SZ14], [SLJ+15], object recognition [SEZ+13] [GDDM14] [HZRS14]. They were also shown capable of per-pixel tasks, such as semantic segmentation [NDL+05] [GGAM14], depth estimation from a single image [LSLR16], optical flow estimation [FDI+15].

Network architecture is a choice that needs to be made a priori. To best of our knowledge, there is no clear guideline on how to choose a network architecture for a new task. We experiment with two network architectures:

- the ZF [ZF13] object recognition network. This is a more traditional CNN architecture.
- the FlowNet [FDI+15] optical flow estimation network. This architecture adheres to a newer fully-convolutional family of networks. These are known to train better and have less parameters vs. their fully-connected counterpart networks.

The input to our network is a pair of subsequent images. A decision to make is how to input the images into the network. There are two common choices: either create two siamese branches, so that each gets its own input image, or to create a single multi-channel image. [FDI+15] show that the latter works equally well while being simpler, so we choose to concatenate the images along the channel dimension to produce a single 6-channel (for color) or 2-channel (for gray-scale) image.

3.4.1 ZF

The network architecture consists of five convolutional and three fully connected layers. Table 3.1 summarizes the architecture.

Layer	**Receptive Field Size**	**Padding**	**Stride**	**Number of Channels**
conv1	7×7	2	3	96
conv2	5×5	2	2	256
conv3	3×3	1	1	384
conv4	3×3	1	1	384
conv5	3×3	1	1	256
fc6				4096
fc7				4096
fc8				1

Table 3.1: ZF network geometry

The flow of data through the network is shown in Figure 3.1. There is a last fully connected layer that reduces a network to a single output, which we are interested to

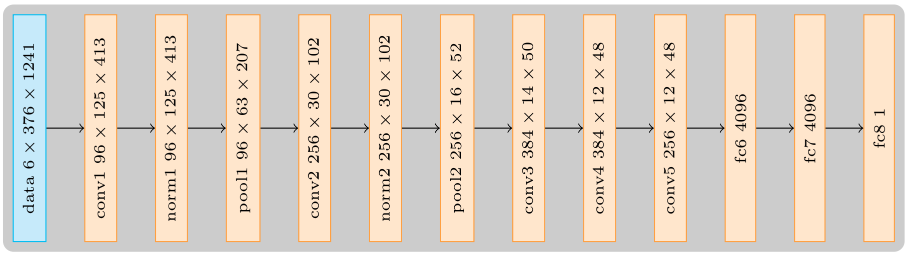

Figure 3.1: ZF network data flow. Each rectangle depicts a top blob for a corresponding layer.

learn. We use euclidean loss to train the network. Total number of parameters is about 624 million.

3.4.2 FlowNet

Fully-convolutional network is a recent trend in the field. They are known to train better and have less parameters vs. their fully connected counterparts [LSD15]. The geometry of the network is described in Table 3.2. Each convolutional layer is followed by the non-linearity. We chose this architecture since it proved successful for optical flow estimation task and has pre-trained model readily available.

Layer	Receptive Field Size	Padding	Stride	Number of Channels
conv1	7×7	3	2	64
conv2	5×5	2	2	128
conv3	5×5	2	2	256
conv3-1	3×3	1	1	256
conv4	3×3	1	2	512
conv4-1	3×3	1	1	512
conv5	3×3	1	2	512
conv5-1	3×3	1	1	512
conv6	3×3	1	2	1024
conv6-1	3×3	1	1	1024
conv7	3×3	1	2	1

Table 3.2: Geometry of the FlowNet based network

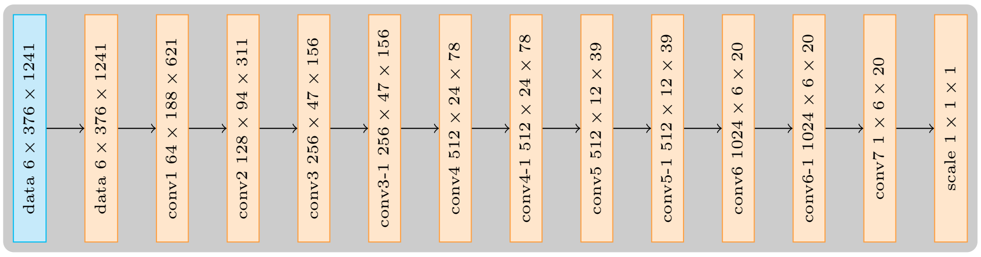

We use Euclidean loss to train the network. The total number of parameters is 24 million.

3.5 Recurrent Neural Networks

Many problems require passing information through time. Since the traditional neural networks are stateless, they are poorly suited for this purpose. Recurrent Neural Networks have loops in them, so that the information can persist.

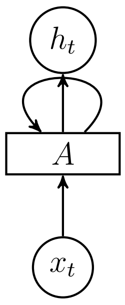

Figure 3.2: RNN

In the Figure 3.2 network A accepts input x_t and outputs h_t. The loop allows the network to pass information from one step of to another.

The RNN may be thought of as a chain of multiple copies of the same neural network where each node passes a message to its successor. This is called *network unrolling*, depicted in Figure 3.3. Unrolled network stresses the relation of the RNN to the sequential data streams. This is an architecture of choice when modeling such data.

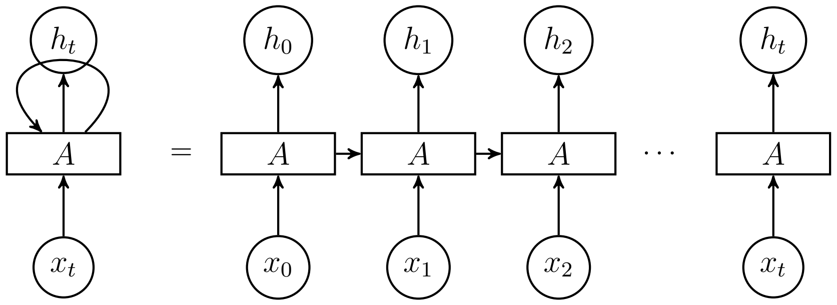

Figure 3.3: Unrolled Recurrent Neural Network

It turns out that the vanilla RNN are hard to train due to the exploding/imploding gradients. Fortunately, Long Short Term Memory Networks (LSTM), which is a special kind of RNN addresses these issues.

LSTM were introduced by [HS97], they are specifically designed to model long term dependencies. Similarly to RNN, LSTM posses a chain-like structure. Each repeating node has an internal structure depicted in Figure 3.4.

The key to the LSTM is a conveyor-like cell state C_t that goes through all cells. Each cell may alter the cell state. The first step is to decide what information we are going to make use of in the cell state C_{t-1}. This is done by a sigmoid "forget gate" layer (Equation 3.4). The "forget gate" looks at the previous output h_{t-1} and the current input x_t and outputs a number in $[0, 1]$ for every cell state component. 0 means completely forget this component and 1 means completely make use of it.

$$f_t = \sigma(W_f[h_{t-1}, x_t] + b_f) \tag{3.4}$$

Next, LSTM makes a step toward the cell state update. The "input gate layer" outputs a number in $[0, 1]$ for each cell state component (similarly to the forget gate, see equation 3.5) and the "tanh" layer computes a cell state update candidate vector (equation 3.6):

$$i_t = \sigma(W_i[h_{t-1}, x_t] + b_i) \tag{3.5}$$

$$\tilde{C_t} = tanh(W_C[h_{t-1}, x_t] + b_C) \tag{3.6}$$

Cell state is updated by "forgetting" some of the information (as decided by the "forget gate") and by adding some new information (governed by the "input gate" and the "tanh"):

$$C_t = f_t * C_{t-1} + i_t * \tilde{C_t} \tag{3.7}$$

Now LSTM decides on its output. The output is based on the cell state

$$o_t = \sigma(W_o[h_{t-1}, x_t] + b_o) \tag{3.8}$$

$$h_t = o_t * tanh(C_t) \tag{3.9}$$

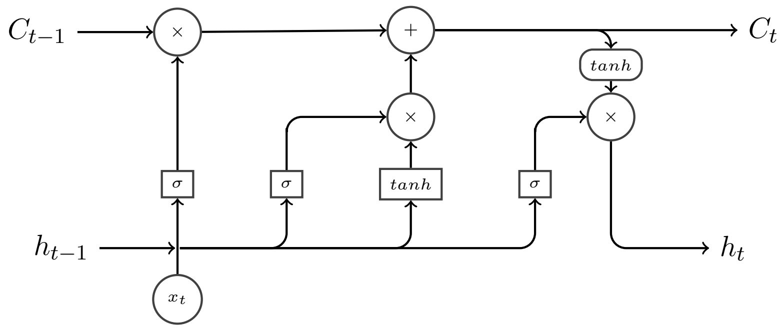

Figure 3.4: LSTM Node

We combine the sequential strengths of the LSTM with convolutional networks. We use our FlowNet (see 3.4.2) as feature extractor. The convnet receives as input a sequence of image pairs and produces a sequence of x_t feature vectors, which are used by the LSTM to produce the output sequence. The convnet and the LSTM are trained jointly.

3.6 Experiments

3.6.1 Data-set

We train and test on the KITTI data-set [GLSU13]. The data-set consists of 11 sequences with ground truth data. We arbitrarily use sequence 00 for testing and sequences 01-10 for training. There are 4540 and 14950 images in the test and the train sets respectively. We only use the data from the left color camera. Figure 3.5 depicts the distribution of the scale values over the train and the test sets.

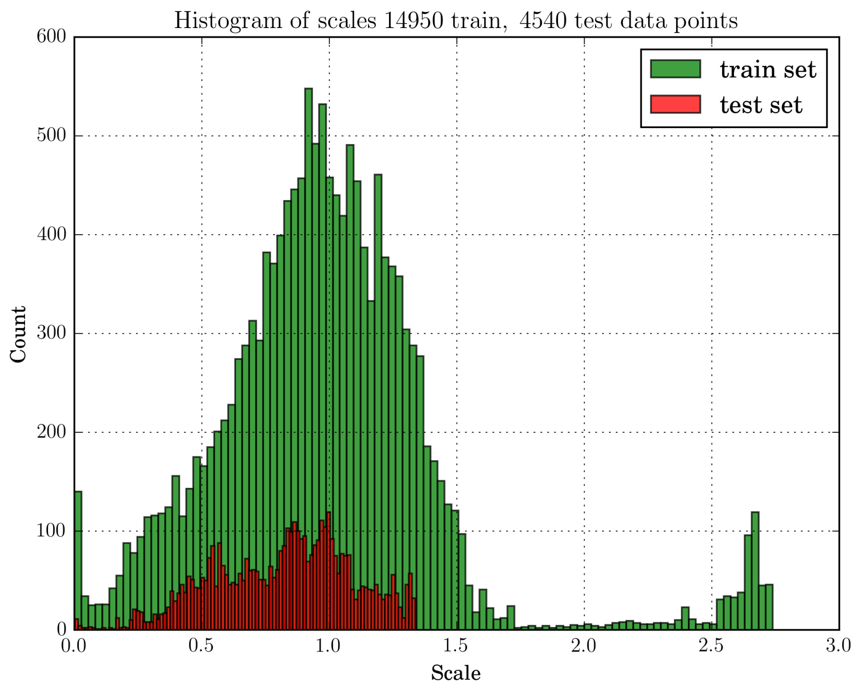

Figure 3.5: Scale distributions

3.6.2 Random Forest

Training a random forest regressor requires hand crafted feature extraction. We convert subsequent image pairs to feature vectors as follows: we extract and match sparse salient points in both input images. The output of this stage is a set of a corresponding pixel locations. For each salient feature we compute the spacial displacement magnitudes (e.g., sparse optical flow). We define a grid in the image space and assign each salient point to a bin. Next, we create histogram of displacement magnitudes for each bin. Concatenating all histograms together produces a feature vector. We use Harris corners and square 11×11 patches as corner descriptors. Sum of square differences is used as a distance measure with the winning pair declared a match. To prune the outliers we fit the fundamental matrix into the matched corner sets and remove the corners that do not agree with the model. Figure 3.6 shows a typical example of extracted and matched corners.

Figure 3.7 depicts the statistics of the feature vectors extracted from the training data. One can see the peaks, that correspond to a closer image regions have a distributions shifted to the right (i.e., larger displacements) and the peaks that correspond to a regions farther away should be closer to zero. This behavior can be observed especially well for the feature vectors that correspond to larger camera displacements (e.g. Figure 3.7c). This figure is an insight why we chose this particular type of feature vector: the distribution of the deisplacements depends on the size of the camera motion.

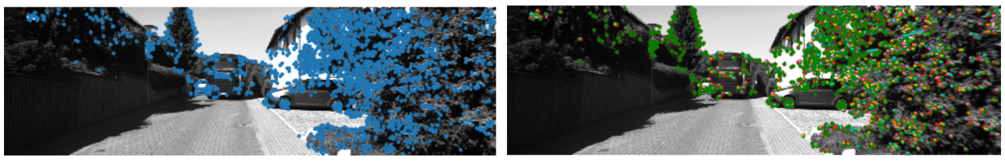
(a) (b)

Figure 3.6: Typical corner extraction and matching. Figure a shows the raw extracted corners, while Figure b shows pruned and matched corners.

We bin each image into 6 × 4 grid. For each bin in the image we compute the histogram of corner disparities. By disparity we denote the displacement of the corner in the image. We use 300-bin histogram for disparities (e.g, feature vector length is 7200). We experimented with different values for the grid size, number of histogram bins and number of random trees in the forest. Aforementioned set of parameters was found empirically to give the best results over the validation set.

We use the extracted features to fit a random forest of 100 trees, by means of recursive node splitting with sub-node variance minimization. We use scikit-lean [PVG+11] random forest implementation. As one may see in Table 3.3, random forest exibits a very low training error/variance but has weaker generalization ability, as opposed to deep models. One reason for this may be that the features are not discriminative enough, i.e., the feature vectors for two image pairs are very close while the scale of the motion is distant.

See Section 3.6.4 for random forest test inference results.

3.6.3 Neural networks

We use Caffe [JSD+14] framework on a single NVIDIA Titan X to train and test our models. For brevity, we elaborate on the training details only for the FlowNet, since it attains best results.

ZF We train using vanilla SGD for 100 epochs. Learning rate is initialized to 1e-5 and decreases by factor of .1 every 10 epochs. We train the network from scratch.

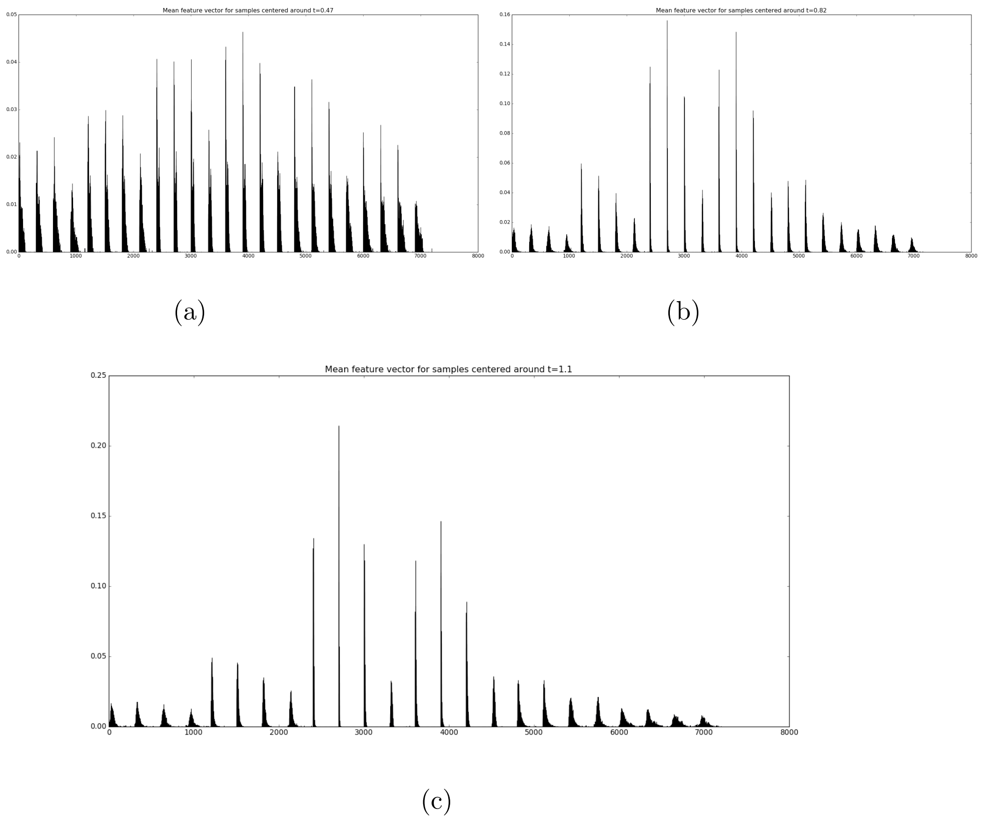

Figure 3.7: Average feature vectors (see 3.6.2) for samples centered around the specific camera translation magnitude. Each peak corresponds to a grid cell (e.g., here the grid is 4 rows by 6 columns by 300 bins, so the feature vector has 6*4*300=7200 dimensions). The grid is sampled in a column-major mode. So the first four peaks correspond to the leftmost column of the image grid.

FlowNet We train using vanilla SGD for 100 epochs. Learning rate is initialized to 1e-5 and decreases by factor of .1 every 10 epochs. We start from pre-trained weights of [FDI$^+$15]. The training proceedes with minibatch size of 5. Train loss graph is shown in 3.8. It may be that we proceed with training after the loss stopped decreasing, but it seems that 100 epoch training time is widely used in the literature. Also, note that the loss is periodic, which happens because of multi-epoch training.

LSTM We also train using vanilla SGD for 100 epochs decreasing learning rate by .1 every 10 epochs. We fine-tune from our FlowNet trained CNN trained weights.

Table 3.3 summarizes trained model error on the training set. This table shows that while random forest succesfully overfits the data, it has a limited generalization ability.

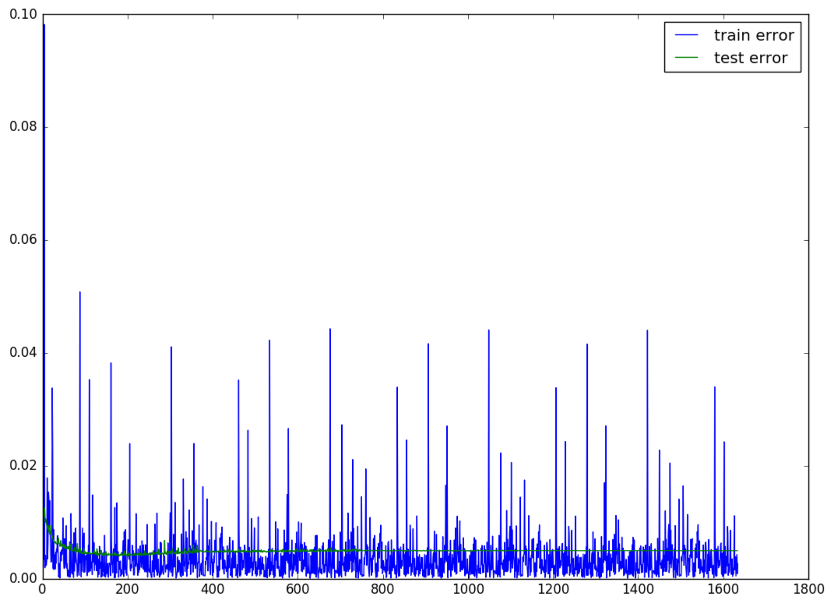

Figure 3.8: FlowNet train loss vs. test loss

	Random Forest	FlowNet
μ_{abs}	5.79e-06	.056
σ_{abs}	1.40e-05	.062
μ	4.88e-15	-2.28e-4
σ	1.51e-05	.083

Table 3.3: Training errors (in meters)

3.6.4 Results

Let the ground truth sequence of camera motion scales be $\{y_i\}_{i=1}^N$, the predicted scales for the same sequence be $\{\hat{y}_i\}_{i=1}^N$, and the corresponding error sequence $\{\delta_i\}_{i=1}^N$:

$$\delta_i = y_i - \hat{y}_i, \tag{3.10}$$

We report two results, the first one is a signed error mean similar to the work of [FMP17]:

$$\mu = \frac{1}{N}\sum_{i=1}^{N}\delta_i, \tag{3.11}$$

The second result is the absolute error mean:

$$\mu_{abs} = \frac{1}{N}\sum_{i=1}^{N}|\delta_i|, \tag{3.12}$$

The μ_{abs} and the σ_{abs} show how close the estimates are to the ground truth values.

The μ shows how biased the estimator is. We report corresponding standard deviations, as well, in Table 3.4. Best result in each category is highlighted in bold. FlowNet exibits minimal absolute error and lowest variance. This is our model of choice. Note that random forest has best signed mean error, but is noisy.

	Random Forest	ZF	FlowNet	LSTM FlowNet	[FKM16]
μ_{abs}	.237	.200	**.078**	.097	
σ_{abs}	.229	.161	**.061**	.074	
μ	**-1.44e-3**	-.007	.023	.017	.014
σ	.329	.257	**.098**	.121	.177

Table 3.4: Experimental Results (in meters)

Our FlowNet produces predictions that have errors of lower variance but are a bit less accurate than [FMP17].

Figure 3.9 and Figure 3.10 shows FlowNet and random forest scale predictions overlayed with the ground truth values for the first 750 frames of the test sequence. The prediction is unbiased and noisy, clearly follows the trend of the ground truth values. Random Forest predictions are a lot more noisy than those of the FlowNet.

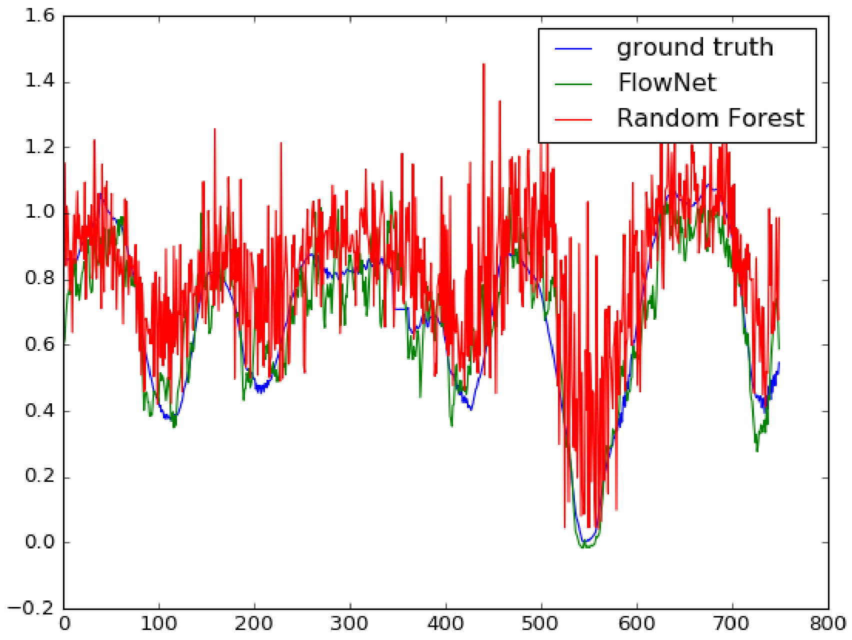

Figure 3.9: FlowNet, Random Forest predictions vs. the ground truth

We perform an additional Kalman Filter step to smooth the predictions. We use constant acceleration model. To estimate the measurement and the process noise we use sequence 02 as a validation set (see e.g., Figure 3.11). In this case the filter merely smoothes the result and keeps the mean errors at the same level. We do suggest that at

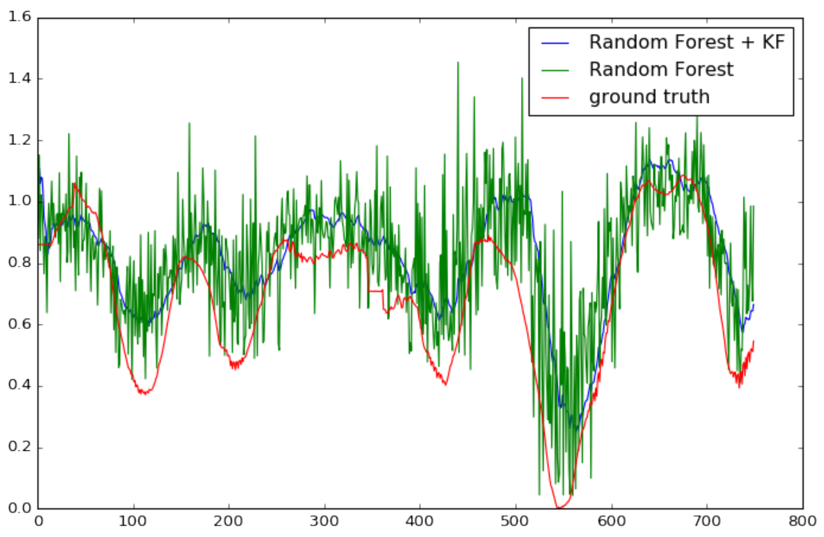

Figure 3.10: Random Forest prediction vs. ground truth

least for some trajectories the Kalman Filter may improve the overall result, since it provides a physical constraint on camera behavior. The neural networks are known to give erroneous output when the test data is far from the train data. These are also the cases where the filter may be beneficial. The result of applying Kalman Filter to both Random Forest and FlowNet predictions is in Figure 3.13 and Figure 3.12, respectively.

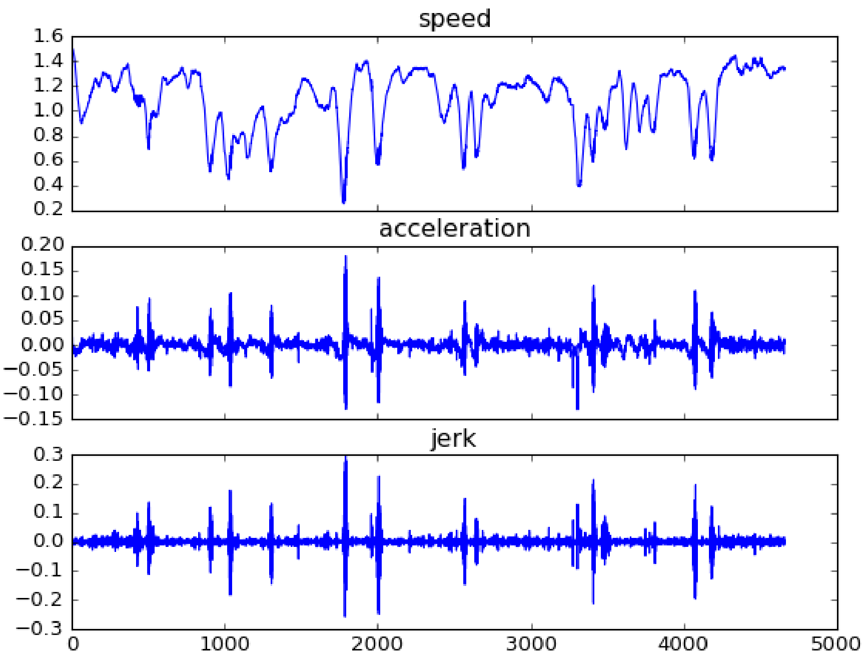

Figure 3.11: KITTI sequence 02 vehicle speed, acceleration and jerk

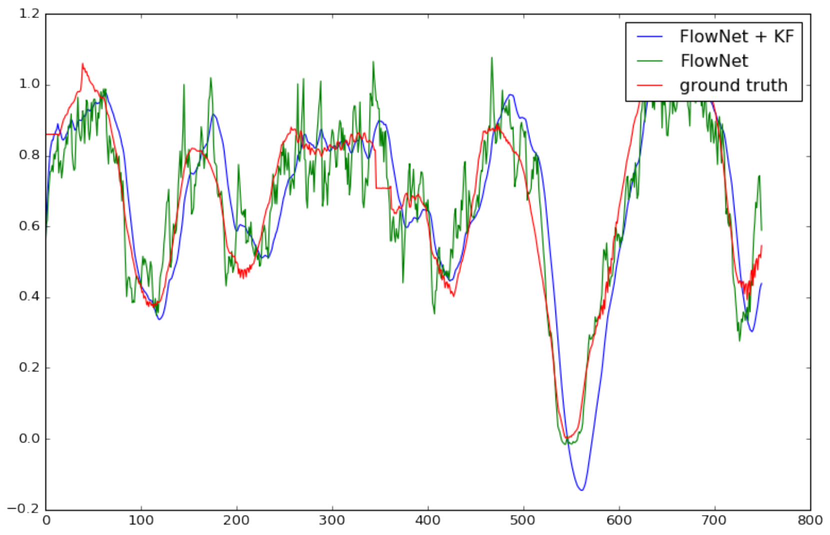

Figure 3.12: FlowNet prediction vs. ground truth vs. Kalman Filter

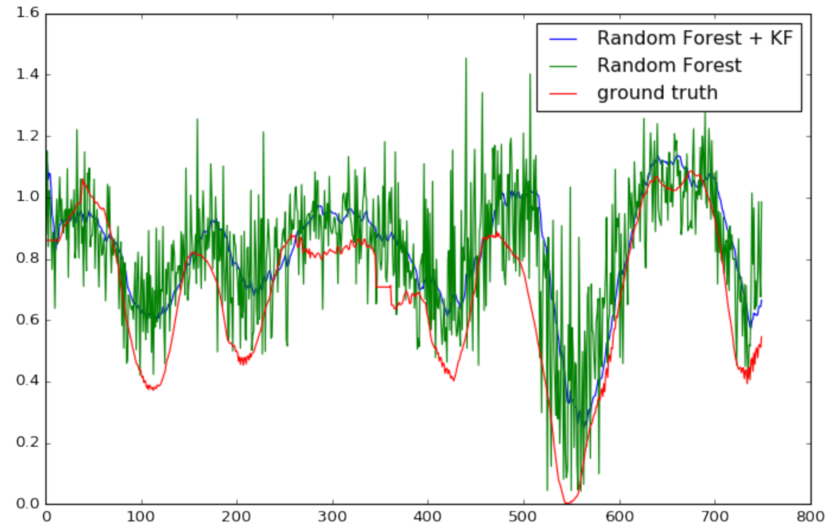

Figure 3.13: Random Forest prediction vs. ground truth vs. Kalman Filter

Finally, we show how our scale affects motion estimation. Let a N-step path of a camera be described by a sequence of homegeneous rigid poses $\{T_i\}_{i=0}^{N}$ as described in Section 3.2.1. In the current context each T_i relates the i-th pose of the camera to the beginning of the path (i.e., pose T_0). Also, denote the corresponding scale estimates by $\{s_i\}_{i=0}^{N}$. We construct a new path $\{\tilde{T}_i\}_{i=0}^{N}$ by rescaling each relative pose appropriately.

First we compute a pose that relates camera $i-1$ to camera i:

$$\Delta T_i = T_{i-1}^{-1} T_i, \tag{3.13}$$

We initialize a rescaled relative pose to be identical to Eq. 3.13

$$\Delta\tilde{T}_i = \Delta T, \tag{3.14}$$

We rescale the relative pose according to be the new scale (array indexing follows Python numpy):

$$\Delta\tilde{T}_i[:3,3] = s_i * \frac{\Delta T_i[:3,3]}{\|\Delta T_i[:3,3]\|}, \tag{3.15}$$

Finally, we constuct a new pose $\tilde{i}$:

$$\tilde{T}_i = \tilde{T}_{i-1} * \Delta\tilde{T}_i, \tag{3.16}$$

We use the above method to rescale the ground truth 00 sequence path according to raw scale estimation and a Kalman-smoothed one. The results are in Figure 3.15 and in Figure 3.14.

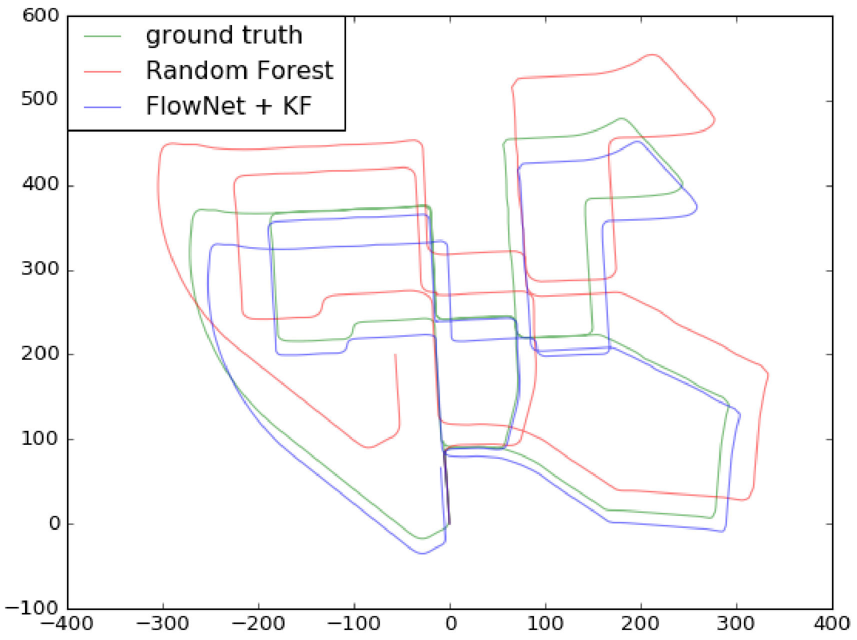

Figure 3.14: Motion estimation, based on the Random Forest predictions

3.7 Conclusions and Discussion

This works presents a data driven approach for monocular scale estimation. We take a holistic path and learn the task end-to-end, rather than splitting it into different sub-tasks.

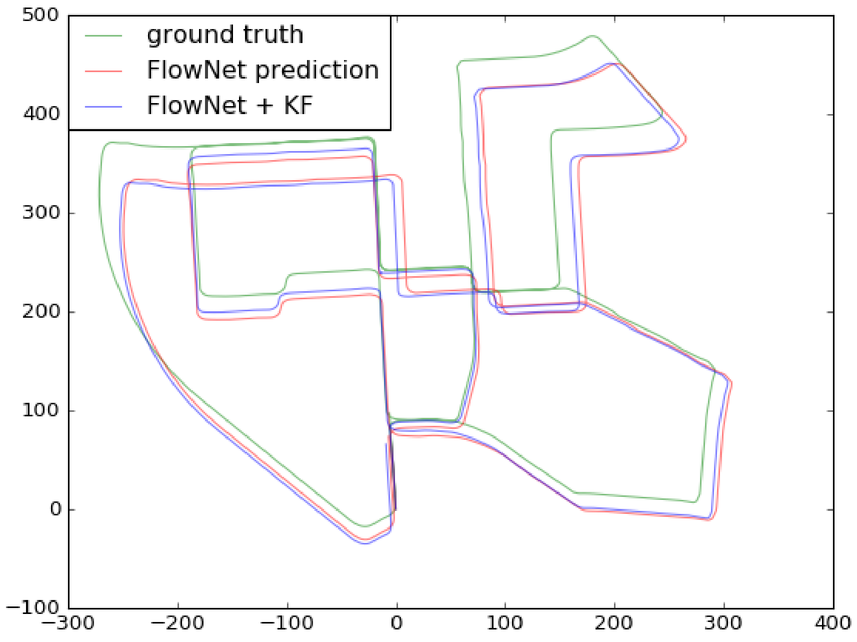

Figure 3.15: Motion estimation, based on the FlowNet predictions

We experimented with both “shallow” random-forest approach and more recent deep learning methods. Deep methods seem to outperform random forest consistently.

We experiment with a number of deep architectures. We learned that the fully convolutional architecture performs better than the traditional (fully-connected layer based) networks. The use of pre-trained weights from the flow-network significantly improves the results.

The network performs about the same if trained on RGB or gray images. We explored different ways for data augmentation, e.g, train the network on images of the right camera as well as the left camera, train on image pairs that are not strictly subsequent, but did not find significant improvement.

Our results show that statistical machine learning is a viable candidate for monocular scale estimation. The (independent) work of [FMP17] also shows that it may be used to produce scale drift free reconstructions. These methods hav a benefit of not-making scene, camera pose assumptions, which may render them as more widely applicable in the future. In this work we deliberately did no scale refinement or blending with other scale estimation methods, to show clearly what the convnets are capable of in this specific context.

Surprisingly, LSTM did not do better than convnets, which is against our expectations. The reason may be that we did not find a proper way to train it.

The main challenge is how to go beyond a purely supervised approach and better utilize the abundance of information that is present in the images to get better predictions.

Chapter 4

Conclusion

This work treats two related sub problems in the field of vision aided navigation.

The first part is of geometric nature and attempts to provide a new insight into stereo and monocular motion estimation. We show that if one is able to split the image points into disjoint sets of near and distant points, then we provide an estimation procedure for camera motion. Our algorithm is local by design and compares favorably to its baseline. By local we mean, that it does not build a map of the environment and thus all its decisions are based on a pair of frames that it sees. Of course, there are larger SLAM systems that give better accuracy overall. Our algorithm may be used as a building block of such systems or may be applicable in the compute-restrained environment.

The second part of our work takes a statistical machine learning approach, which leverages available data and compute power to solve the visual navigation scaling problem. We show how to train a model to provide unbiased and low-variance scale estimates. We also show a simple approach which uses our scale estimates to provide full 6-DOF motion estimation. The work of [FMP17] show a different, more complex way to do motion estimation based on similar scale estimates. While the current result allows for scale drift free motion estimation we feel that it may be greatly improved by better use of the available data.

In recent years the field of visual navigation has matured research-wise. It seems that most of the important fundamental questions are answered. Said that, there still is a significant gap between state of the art and real world systems that rely on visual data. Part of this gap is in engineering, which is complex (most real world systems use additional modalities: lidars, depth sensors, etc.). We speculate that another part of the gap is that in order to navigate in complex (e.g., urban) environments one can not rely on geometric information alone and semantic understanding of the scene is needed.

It also seems that the field is ready to take on larger-scale problems, such as motion estimation and mapping on a very large scale, collaborative large-scale mapping and navigation. We feel that (at least near-future) algorithms should leverage the power of traditional geometry based approaches with a more recent data-driven methods.

One thing that we find very important is the appearance of new and more challenging data sets. KITTI, while being a great data set is low in its lighting, weather conditions, scenery and traffic variability. We hope that the recent spree of the autonomous driving companies will lead to the appearance of such new data sets, which in turn, will foster new research.

Bibliography

[BTG06] Herbert Bay, Tinne Tuytelaars, and Luc Van Gool. SURF: speeded up robust features. In *In ECCV*, pages 404–417, 2006.

[BYK13] Hernán Badino, Akihiro Yamamoto, and Takeo Kanade. Visual odometry by multi-frame feature integration. *Proceedings of the IEEE International Conference on Computer Vision*, pages 222–229, 2013.

[CCVR14] Thomas A. Ciarfuglia, Gabriele Costante, Paolo Valigi, and Elisa Ricci. Evaluation of non-geometric methods for visual odometry. *Robotics and Autonomous Systems*, 62(12):1717 – 1730, 2014.

[FDI+15] Philipp Fischer, Alexey Dosovitskiy, Eddy Ilg, Philip Häusser, Caner Hazırbaş, Vladimir Golkov, Patrick van der Smagt, Daniel Cremers, and Thomas Brox. Flownet: Learning optical flow with convolutional networks. *arXiv preprint arXiv:1504.06852*, 2015.

[FKM16] Duncan P Frost, Olaf Kähler, and David W Murray. Object-aware bundle adjustment for correcting monocular scale drift. In *Robotics and Automation (ICRA), 2016 IEEE International Conference on*, pages 4770–4776. IEEE, 2016.

[FMP17] Duncan P Frost, David W Murray, and Victor A Prisacariu. Using learning of speed to stabilize scale in monocular localization and mapping. In *2017 International Conference on 3D Vision (3DV)*, 2017.

[FS12] Friedrich Fraundorfer and Davide Scaramuzza. Visual odometry: Part ii: Matching, robustness, optimization, and applications. *IEEE Robotics & Automation Magazine*, 19(2):78–90, 2012.

[FSBM17] N. Fanani, A. Sturck, M. Barnada, and R. Mester. Multimodal scale estimation for monocular visual odometry. In *2017 IEEE Intelligent Vehicles Symposium (IV)*, pages 1714–1721, June 2017.

[GDDM14] Ross Girshick, Jeff Donahue, Trevor Darrell, and Jitendra Malik. Rich feature hierarchies for accurate object detection and semantic segmentation. In *Proceedings of the IEEE conference on computer vision and pattern recognition*, pages 580–587, 2014.

[Gei12] Andreas Geiger. Are we ready for autonomous driving? the kitti vision benchmark suite. In *Proceedings of the 2012 IEEE Conference on Computer Vision and Pattern Recognition (CVPR)*, CVPR '12, pages 3354–3361, Washington, DC, USA, 2012. IEEE Computer Society.

[GGAM14] Saurabh Gupta, Ross Girshick, Pablo Arbeláez, and Jitendra Malik. Learning rich features from rgb-d images for object detection and segmentation. In *European Conference on Computer Vision*, pages 345–360. Springer, 2014.

[GGPG12] Daniel Gutiérrez-Gómez, Luis Puig, and José Jesús Guerrero. Full scaled 3d visual odometry from a single wearable omnidirectional camera. In *Intelligent Robots and Systems (IROS), 2012 IEEE/RSJ International Conference on*, pages 4276–4281. IEEE, 2012.

[GLSU13] Andreas Geiger, Philip Lenz, Christoph Stiller, and Raquel Urtasun. Vision meets robotics: The kitti dataset. *The International Journal of Robotics Research*, 32(11):1231–1237, 2013.

[Gov09] Natasha Govender. Evaluation of Feature Detection Algorithms for Structure from Motion. *CSIR tech report*, 2009.

[GR13] Vitor Guizilini and Fabio Ramos. Semi-parametric learning for visual odometry. *The International Journal of Robotics Research*, 32(5):526–546, 2013.

[GSL15] Johannes Gräter, Tobias Schwarze, and Martin Lauer. Robust scale estimation for monocular visual odometry using structure from motion and vanishing points. In *Intelligent Vehicles Symposium (IV), 2015 IEEE*, pages 475–480. IEEE, 2015.

[GZS11] Andreas Geiger, Julius Ziegler, and Christoph Stiller. Stereoscan: Dense 3d reconstruction in real-time. In *Intelligent Vehicles Symposium*, pages 963–968. IEEE, 2011.

[HFF09] Johan Hedborg, Pe Forssén, and Michael Felsberg. Fast and accurate structure and motion estimation. *5th International Symposium on Advances in Visual Computing: Part I*, pages 211–222, 2009.

[Hor87] Berthold K P Horn. Closed-form solution of absolute orientation using unit quaternions. *Journal of the Optical Society of America A*, 4:629, 1987.

[HP87] C G Harris and J M Pike. 3D Positional Integration from Image Sequences. *Procedings of the Alvey Vision Conference 1987*, pages 233–236, 1987.

[HS88] Chris Harris and Mike Stephens. A Combined Corner and Edge Detector. *Procedings of the Alvey Vision Conference 1988*, pages 147–151, 1988.

[HS97] Sepp Hochreiter and Jürgen Schmidhuber. Long short-term memory. *Neural computation*, 9(8):1735–1780, 1997.

[HZ04] R. I. Hartley and A. Zisserman. *Multiple View Geometry in Computer Vision*. Cambridge University Press, ISBN: 0521540518, second edition, 2004.

[HZRS14] Kaiming He, Xiangyu Zhang, Shaoqing Ren, and Jian Sun. Spatial pyramid pooling in deep convolutional networks for visual recognition. In *European Conference on Computer Vision*, pages 346–361. Springer, 2014.

[JSD+14] Yangqing Jia, Evan Shelhamer, Jeff Donahue, Sergey Karayev, Jonathan Long, Ross Girshick, Sergio Guadarrama, and Trevor Darrell. Caffe: Convolutional architecture for fast feature embedding. *arXiv preprint arXiv:1408.5093*, 2014.

[KAS10] Kurt Konolige, Motilal Agrawal, and Joan Solà. Large-scale visual odometry for rough terrain. *Springer Tracts in Advanced Robotics*, 66:201–212, 2010.

[KM07] Georg Klein and David Murray. Parallel tracking and mapping for small ar workspaces. In *Proceedings of the 2007 6th IEEE and ACM International Symposium on Mixed and Augmented Reality*, ISMAR '07, pages 1–10, Washington, DC, USA, 2007. IEEE Computer Society.

[KRC+11] Bernd Manfred Kitt, Jörn Rehder, Andrew D Chambers, Miriam Schonbein, Henning Lategahn, and Sanjiv Singh. Monocular visual odometry using a planar road model to solve scale ambiguity. *Proceedings of the 5th European Conference on Mobile Robots (ECMR 2011), rebro, Sweden, September 7-9, 2011. Ed.: A. J. Lilienthal*, pages 43–48, 2011.

[KRD08] Michael Kaess, Ananth Ranganathan, and Frank Dellaert. iSAM: incremental smoothing and mapping. *IEEE Transactions on Robotics*, 24(6):1365–1378, 2008.

[KSH12] Alex Krizhevsky, Ilya Sutskever, and Geoffrey E Hinton. Imagenet classification with deep convolutional neural networks. In *Advances in neural information processing systems*, pages 1097–1105, 2012.

[KSS11] Laurent Kneip, Davide Scaramuzza, and Roland Siegwart. A novel parametrization of the perspective-three-point problem for a direct computation of absolute camera position and orientation. *Proceedings of the IEEE Computer Society Conference on Computer Vision and Pattern Recognition*, pages 2969–2976, 2011.

[Low04] David G Lowe. Distinctive image features from scale invariant keypoints. *Int'l Journal of Computer Vision*, 60:91–110, 2004.

[LSD15] Jonathan Long, Evan Shelhamer, and Trevor Darrell. Fully convolutional networks for semantic segmentation. In *Proceedings of the IEEE Conference on Computer Vision and Pattern Recognition*, pages 3431–3440, 2015.

[LSLR16] Fayao Liu, Chunhua Shen, Guosheng Lin, and Ian Reid. Learning depth from single monocular images using deep convolutional neural fields. *IEEE transactions on pattern analysis and machine intelligence*, 38(10):2024–2039, 2016.

[MAD$^+$16] Vikram Mohanty, Shubh Agrawal, Shaswat Datta, Arna Ghosh, Vishnu Dutt Sharma, and Debashish Chakravarty. Deepvo: A deep learning approach for monocular visual odometry. *CoRR*, abs/1611.06069, 2016.

[Mor80] Hans Peter Moravec. Obstacle avoidance and navigation in the real world by a seeing robot rover. *tech. report CMU-RI-TR-80-03*, page 175, 1980.

[MS06] Annalisa Milella and Roland Siegwart. Stereo-based ego-motion estimation using pixel tracking and iterative closest point. *Proceedings of the Fourth IEEE International Conference on Computer Vision Systems, ICVS'06*, 2006(Icvs):21, 2006.

[MS17] Peter Muller and Andreas Savakis. Flowdometry: An optical flow and deep learning based approach to visual odometry. In *Applications of Computer Vision (WACV), 2017 IEEE Winter Conference on*, pages 624–631. IEEE, 2017.

[NDL$^+$05] Feng Ning, Damien Delhomme, Yann LeCun, Fabio Piano, Léon Bottou, and Paolo Emilio Barbano. Toward automatic phenotyping of developing embryos from videos. *IEEE Transactions on Image Processing*, 14(9):1360–1371, 2005.

[Nis04] David Nistér. An efficient solution to the five-point relative pose problem. *IEEE Transactions on Pattern Analysis and Machine Intelligence*, 26(6):756–770, 2004.

[NLD11] R A Newcombe, S J Lovegrove, and A J Davison. DTAM: Dense Tracking and Mapping in Real-Time. *Int. Conf. on Computer Vision (ICCV)*, pages 2320–2327, 2011.

[OMSM03] Clark F. Olson, Larry H. Matthies, Marcel Schoppers, and Mark W. Maimone. Rover navigation using stereo ego-motion. *Robotics and Autonomous Systems*, 43(4):215–229, 2003.

[PPFM15] Mikael Persson, Tommaso Piccini, Michael Felsberg, and Rudolf Mester. Robust stereo visual odometry from monocular techniques. *IEEE Intelligent Vehicles Symposium, Proceedings*, 2015-Augus:686–691, 2015.

[PVG$^+$11] F. Pedregosa, G. Varoquaux, A. Gramfort, V. Michel, B. Thirion, O. Grisel, M. Blondel, P. Prettenhofer, R. Weiss, V. Dubourg, J. Vanderplas, A. Passos, D. Cournapeau, M. Brucher, M. Perrot, and E. Duchesnay. Scikit-learn: Machine learning in Python. *Journal of Machine Learning Research*, 12:2825–2830, 2011.

[RD06] Edward Rosten and Tom Drummond. Machine learning for high-speed corner detection. *Computer Vision–ECCV 2006*, 3951 LNCS:430–443, 2006.

[RNKB08] Richard Roberts, Hai Nguyen, Niyant Krishnamurthi, and Tucker Balch. Memory-based learning for visual odometry. In *Robotics and Automation, 2008. ICRA 2008. IEEE International Conference on*, pages 47–52. IEEE, 2008.

[SC14] Shiyu Song and Manmohan Chandraker. Robust scale estimation in real-time monocular sfm for autonomous driving. In *Proceedings of the IEEE Conference on Computer Vision and Pattern Recognition*, pages 1566–1573, 2014.

[SCG13] Shiyu Song, Manmohan Chandraker, and Clark C Guest. Parallel, real-time monocular visual odometry. In *Robotics and Automation (ICRA), 2013 IEEE International Conference on*, pages 4698–4705. IEEE, 2013.

[SEZ$^+$13] Pierre Sermanet, David Eigen, Xiang Zhang, Michaël Mathieu, Rob Fergus, and Yann LeCun. Overfeat: Integrated recognition, localization and detection using convolutional networks. *arXiv preprint arXiv:1312.6229*, 2013.

[SFPS09] Davide Scaramuzza, Friedrich Fraundorfer, Marc Pollefeys, and Roland Siegwart. Absolute scale in structure from motion from a single vehicle mounted camera by exploiting nonholonomic constraints. In *2009 IEEE 12th International Conference on Computer Vision*, pages 1413–1419. IEEE, 2009.

[SLJ$^+$15] Christian Szegedy, Wei Liu, Yangqing Jia, Pierre Sermanet, Scott Reed, Dragomir Anguelov, Dumitru Erhan, Vincent Vanhoucke, and Andrew Rabinovich. Going deeper with convolutions. In *Proceedings of the IEEE conference on computer vision and pattern recognition*, pages 1–9, 2015.

[ST94] Jianbo Shi Jianbo Shi and Carlo Tomasi. Good features to track. *Computer Vision and Pattern Recognition, 1994*, pages 593–600, 1994.

[SZ14] Karen Simonyan and Andrew Zisserman. Very deep convolutional networks for large-scale image recognition. *arXiv preprint arXiv:1409.1556*, 2014.

[TMHF99] Bill Triggs, Philip F McLauchlan, Richard I Hartley, and Andrew W Fitzgibbon. Bundle adjustmenta modern synthesis. In *International workshop on vision algorithms*, pages 298–372. Springer, 1999.

[WCWT17] Sen Wang, Ronald Clark, Hongkai Wen, and Niki Trigoni. DeepVO: towards end-to-end visual odometry with deep recurrent convolutional neural networks. In *Robotics and Automation (ICRA), 2017 IEEE International Conference on*, pages 2043–2050. IEEE, 2017.

[ZDL16] Dingfu Zhou, Yuchao Dai, and Hongdong Li. Reliable scale estimation and correction for monocular visual odometry. In *Intelligent Vehicles Symposium (IV), 2016 IEEE*, pages 490–495. IEEE, 2016.

[ZF13] Matthew D. Zeiler and Rob Fergus. Visualizing and understanding convolutional networks. *CoRR*, abs/1311.2901, 2013.